AGU PUBLICATIONS

JGR

Journal of Geophysical Research: Solid Earth

RESEARCH ARTICLE

10.1002/2016JB012945

Multiple branching rupture of the 2009 Tonga-Samoa earthquake

Wenyuan Fan[1], Peter M. Shearer[1], Chen Ji[2,3], and Dan Bassett[1]

[1]Scripps Institution of Oceanography, University of California, San Diego, La Jolla, California, USA, [2]Earth Research Institute, University of California, Santa Barbara, California, USA, [3]Department of Earth Science, University of California, Santa Barbara, California, USA

Key Points:
- The 2009 Tonga-Samoa earthquake ruptured multiple fault segments with different focal mechanisms
- The rupture of different fault segments shows frequency-dependent behaviors
- The apparent normal-reverse faulting interactions increase the seismic risk in this region

Supporting Information:
- Supporting Information S1

Correspondence to:
W. Fan,
w3fan@ucsd.edu

Citation:
Fan, W., P. M. Shearer, C. Ji, and D. Bassett (2016), Multiple branching rupture of the 2009 Tonga-Samoa earthquake, *J. Geophys. Res. Solid Earth*, *121*, 5809–5827, doi:10.1002/2016JB012945.

Received 22 FEB 2016
Accepted 12 JUL 2016
Accepted article online 18 JUL 2016
Published online 4 AUG 2016

Abstract Several source models have been proposed to explain the enigmatic 2009 Tonga-Samoa earthquake. The long-period data require a composite source model and can be fit with a normal-faulting subevent followed by one or more reverse-faulting subevents. The short-period data, in contrast, indicate a more compact rupture pattern around the epicenter. The lack of a unified source model reflects the complexity of the event. We analyze the spatiotemporal evolution of this earthquake with *P* wave back-projection from globally distributed stations in different frequency bands (low frequency: 0.05–0.2 Hz, high frequency: 0.2–2 Hz) and a multiple moment tensor inversion. The rupture propagation revealed by back-projection exhibits frequency-dependent behavior, with two branches of high-frequency-enriched bilateral rupture around the epicenter and a high-frequency-deficient rupture branch at the subduction interface. A composite source model with one M_w 8.0 normal-faulting earthquake east of the trench axis (seaward) followed by one M_w 8.1 reverse-faulting earthquake along the subduction interface west of the trench axis (landward) can explain the very long period data (200∼500 s). Combined with high-resolution swath bathymetry data, the back-projection images show that the azimuth of rupture branches east of the trench axis were controlled by the geometry of bending-related faults on the Pacific plate and that the rupture branch west of the trench axis may correlate with the along-strike fore-arc segmentation. The rupture along the subduction interface was triggered by the seaward rupture and a partially subducted normal fault may have played a key role in facilitating the triggering. The apparent normal-reverse faulting interactions pose a higher seismic risk to this region than their individual strands at the northernmost corner of the Tonga subduction zone.

1. Introduction

The northern end of the Tonga subduction zone is tectonically complex and a prominent example of tearing plates [*Wilson*, 1965; *Millen and Hamburger*, 1998; *Govers and Wortel*, 2005]. Both seismic observations and geodynamic modeling show that the Pacific plate lithosphere experiences downwarping and tearing as it subducts into the northernmost segment of the Tonga subduction zone [*Millen and Hamburger*, 1998; *Govers and Wortel*, 2005]. Both normal-faulting and reverse-faulting events occur in the northern corner that cannot be explained by simple pulling and bending subduction dynamics (Figure 1). The termination zone has a linear west-east trend that extends ∼ 300 km parallel to the relative Pacific plate motion to the Australian plate. The tearing-induced faults, newly formed outer-rise faults, in conjunction with the preexisting fabric of the Pacific plate, produce complicated fault networks in the region. Residual bathymetry gradients clearly reveal the complexities of this system (Figure 1) [*Bassett and Watts*, 2015a, 2015b]. East (seaward) of the trench axis, bending-related faults exhibit complex along-strike variations in spacing and strike. Bend faults are approximately trench parallel (or N-S) with a mean spacing of ∼ 20 km south of −16.5° and are gradually rotated to be trench perpendicular (E-W) with a mean spacing of ∼5 km north of −15.3°.

The 29 September 2009 Tonga-Samoa earthquake occurred offshore of the northern termination of the Tonga subduction zone. The Global Centroid Moment Tensor (GCMT) [*Ekström et al.*, 2012] solution modeled it as a single point source, with strike 346°, dip 62° to the east, and rake −63°. The finite-fault model from the U.S. Geological Survey National Earthquake Information Center (NEIC) favors a nodal plane with strike 342.5° and dip 57.1°, with bilateral rupture to the surface [*Hayes*, 2011; *Hayes et al.*, 2011; *Ji et al.*, 2002]. The relatively poor waveform fits in the finite-fault modeling indicate that a single-fault model is insufficient to explain the

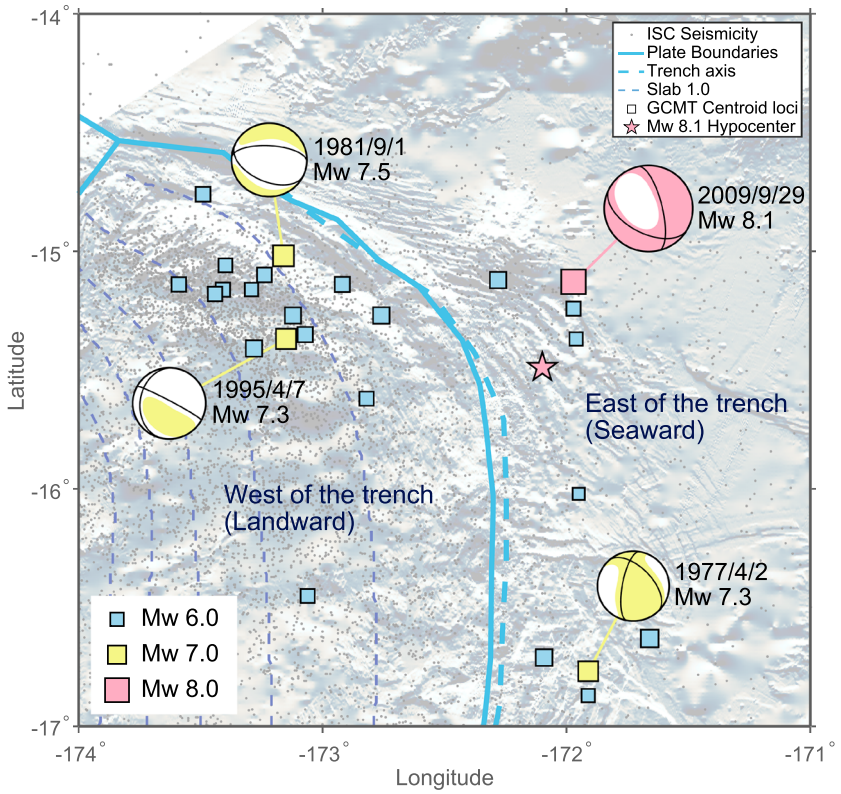

Figure 1. Tectonic setting of the northern corner of the Tonga subduction zone. Seismicity (8274 earthquakes, 1916–2012) is from *International Seismological Centre* [2013]. Focal mechanisms of the $M > 6$ earthquakes with centroid depths shallower than 60 km within the region are shown as squares; $M > 7$ earthquake moment magnitudes are listed by their focal mechanisms [*Ekström et al.*, 2012]. The plate boundary is from *Bird* [2003], trench axis is from *Bassett and Watts* [2015a, 2015b], and the subduction geometry is from Slab 1.0 with 20 km separation [*Hayes et al.*, 2012]. The background bathymetry gradient is from *Sandwell et al.* [2014] and *Garcia et al.* [2014].

observations and several more complex models have been proposed. It was first reported by *Li et al.* [2009] that the earthquake was composed of both a normal-faulting main shock and an additional "hidden" triggered thrust event, based on analysis of teleseismic body waves, surface waves, and local strong motion data. *Lay et al.* [2010] found evidences for a normal-faulting main shock, closely followed by two triggered reverse-faulting events, based on analysis of R1 source-time functions (STFs), array back-projection and surface wave modeling. *Beavan et al.* [2010] proposed a two-fault model, with a slow-slip event at the subduction zone before the normal-faulting main shock, based on GPS near-field observations and Deep-ocean Assessment and Reporting of Tsunamis buoy observations. *Kiser and Ishii* [2012] argued that there were at least two subevents composing the earthquake, which were spatially focused around the epicenter, based on USArray and Hi-Net combined array back-projection. *Duputel et al.* [2012] and *Nealy and Hayes* [2015] independently confirmed the normal-reverse doublet with *W* phase inversion, agreeing well with the focal mechanisms, while showing variations in the locations and timing of the two events. These studies make clear that the Tonga-Samoa earthquake was complicated, with at least two major subevents, but there is not yet consensus on the subvent locations and other details, which hampers understanding of the rupture dynamics and its relation to structures in the region.

These uncertainties motivate this study. We comprehensively investigate the Tonga-Samoa earthquake rupture process with broadband far-field seismic observations, quantify the resolved source model uncertainties with various tests, and explore possible physical causes of the observed rupture pattern in conjunction with local tectonics. For the high- and low-frequency bands, we apply *P* wave back-projection to image the spatiotemporal behavior of the earthquake. For very long period data, we model the earthquake with multiple point sources with different moment tensor solutions to fit the initial 5400 s of the waveforms. To evaluate intrinsic ambiguities in the imaging approaches (e.g., back-projection and moment tensor inversion) and to understand the variations among the available source models, we apply a number of tests to assess the

uncertainty and resolution of back-projection and explore the spatiotemporal resolving limits of moment tensor inversion by grid searching the model space. We show that all the data for the 2009 Tonga-Samoa earthquake can be reasonably explained with a unified multiple branching rupture model and quantify its uncertainty and resolution. Comparisons with seafloor bathymetry suggest that the multiple branching rupture is a natural consequence of the fault geometry and the fore-arc material segmentation.

First introduced by *Ishii et al.* [2005] for the 2004 Sumatra earthquake, the back-projection method has proven useful in studying complex ruptures because it makes few a priori assumptions about the fault geometry. High-frequency regional array data, such as Hi-net or USArray, are often used for back-projection imaging because of their good waveform coherence [e.g., *Kiser and Ishii*, 2011; *Wang et al.*, 2012; *Meng et al.*, 2011; *Koper et al.*, 2011; *Satriano et al.*, 2012; *Fan and Shearer*, 2016]. However, the superior azimuthal coverage of globally distributed stations can provide better resolution than regional arrays [e.g., *Walker et al.*, 2005; *Walker and Shearer*, 2009; *Yagi et al.*, 2012; *Okuwaki et al.*, 2014; *Fan and Shearer*, 2015]. Following *Fan and Shearer* [2015], we analyze both a high-frequency band (0.2 to 2 Hz), similar to that used most often in prior back-projection studies, and a low-frequency band (0.05 to 0.2 Hz) to provide a more complete description of the seismic radiation. In addition, we solve for centroid moment tensor (CMT) models [*Gilbert*, 1971; *Dziewoński et al.*, 1981; *Ekström et al.*, 2012] to constrain the average fault geometry and moment release, based on fits to very long period (200 s – 500 s) body and surface waves.

Our results suggest that the rupture had at least three fault branches, with an initial northwestward rupture branch along a curved normal fault, followed by a southeastward rupture branch along the same fault, and a southward final rupture branch at the subduction interface. The first two branches can be characterized as a M_w 8.0 bilateral-rupturing normal-faulting earthquake, which agrees with GCMT, single-point *W* phase CMT [*Duputel et al.*, 2012b; *Nealy and Hayes*, 2015] and NEIC finite-fault solutions. The third rupture branch is depicted by a M_w 8.1 reverse-faulting event with a shallow dip angle, which agrees with other double CMT models [*Li et al.*, 2009; *Duputel et al.*, 2012; *Nealy and Hayes*, 2015]. Possible early aftershocks are triggered immediately after the main shock within 2 min. Integrating our results with the aftershock distribution, currently available source models, and local bathymetry data, we conclude that the earthquake consisted of two *M*8 subevents, with at least three fault segments involved. The reverse-faulting rupture branch was triggered by the rupture branches east of the trench. Across the trench, a partially subducted normal fault is revealed by high-resolution swath bathymetry data, which might link faults across the trench axis, and facilitate the initiation of the second subevent at the megathrust. Finally, we discuss the frequency-dependent rupture behavior of this event and compare our results with source models of the 2006 – 2007 Kuril Islands earthquakes doublet to infer general characteristics of this type of multifault earthquake sequence.

2. Method and Data

2.1. Back-Projection

Assuming that the *P* waves are representative of the earthquake rupture process with little distortion during wave propagation, the back-projection method aligns, shifts, and stacks seismograms to extract coherent signals which serve as approximations for the radiation from hypothesized source locations relative to the hypocenter. For a grid of possible source points, the aligned seismograms will constructively interfere for true source locations or destructively interfere for other points. We closely follow the method described in *Walker et al.* [2005] and *Fan and Shearer* [2015], with *N*th root stacking [*Xu et al.*, 2009] to suppress noise. Seismograms are first aligned using theoretical *P* wave traveltimes calculated with a 1-D velocity model (IASP91) [*Kennett and Engdahl*, 1991]. We then apply empirical time shifts to account for 3-D velocity structure by aligning the initial 5 s of the *P* arrival [*Houser et al.*, 2008] with allowed time shifts of ±4 s, assuming it comes from the hypocenter (Figure S1 in the supporting information). No polarity flips are allowed during the alignment, since all the stations used for back-projection share the same *P* wave polarities (Figure 2). In principle, the source locations could be three-dimensional, but because of poor depth sensitivity, we focus only on lateral variations in this study and grid potential source locations as functions of latitude and longitude with depth fixed to the hypocentral depth (18 km). Nonlinear stacking approaches, like *N*th root stacking [*Rost and Thomas*, 2002], have been successfully applied to back-projection to sharpen signals and suppress noise [*Xu et al.*, 2009], at the cost of absolute amplitude information. In this study, we use $N = 4$ as suggested in *Xu et al.* [2009] and discussed in *McFadden et al.* [1986].

The potential sources are gridded at 5 km spacing, within the latitude range −17.28° to −13.69° and longitude range −173.96° to −170.23° (400 km by 400 km). We use vertical-component velocity records from

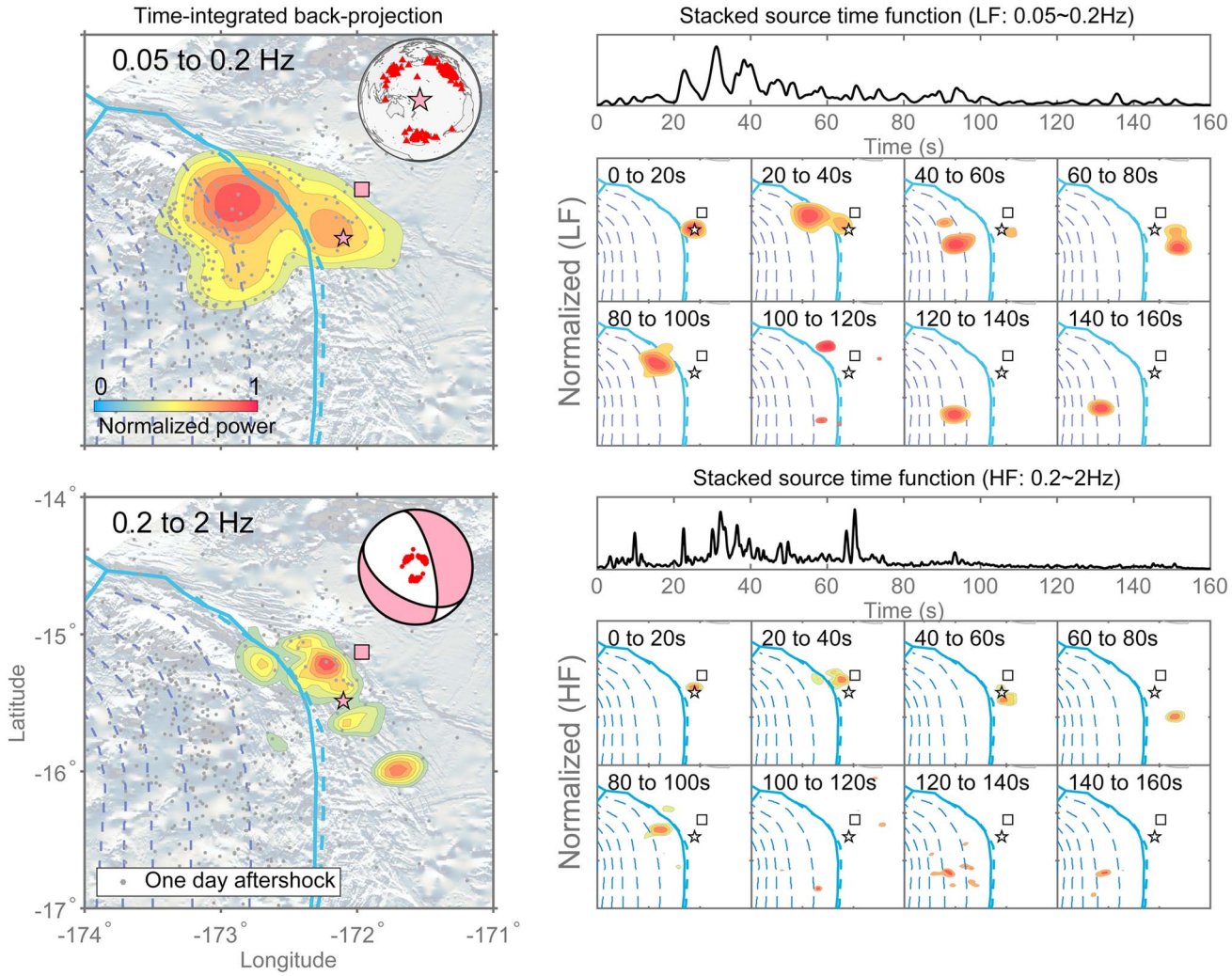

Figure 2. Back-projection results. (top row) Low-frequency (LF, 0.05–0.2 Hz) time-integrated back-projection image, stacked source-time function and time snapshots. (bottom row) High-frequency (HF, 0.2–2 Hz) time-integrated back-projection image, stacked source-time function, and time snapshots. Stations used for the back-projection analysis are mapped in the upper right corner of the integrated LF back-projection image, with their lower focal hemisphere polarities plotted in the upper right corner of the integrated HF back-projection image.

global broadband stations distributed by the Data Management Center (DMC) of Incorporated Research Institutions for Seismology (IRIS) (Figure 2). One hundred and sixteen stations with high signal-to-noise ratios are hand-selected to perform the back-projection. The epicentral distances are limited to from 44° to 90° to avoid waveform complexities introduced by mantle discontinuities. The azimuth ranges from 10.6° to 353.38° (Figure 2), which greatly enhances the back-projection spatial resolution and suppresses artifacts. To investigate possible frequency dependence in the seismic radiation, we examine three different frequency bands, 0.05–0.2 Hz (low frequency, LF), 0.1–1 Hz (middle frequency, MF), and 0.2–2 Hz (high frequency, HF). Back-projection for each band uses the same alignment, obtained from cross correlating the first 5 s of the LF data (Figure S1). The LF and HF results are described in the main paper; the MF results are presented in the supporting information.

To avoid biasing the back-projection results, the records are normalized to unit amplitude to remove variations caused by site effects, radiation pattern, and different instrument gains. They are also weighted by their average correlation coefficients with the waveform stack during cross correlation (to down-weight noisy records) and inversely by the number of contributing stations within 5° (to reduce the relative influence of large numbers of stations in a single region). No postsmoothing or postprocessing is applied to the images.

2.2. Multiple Moment Tensor Inversion

The moment tensor (MT) is a point source representation for earthquakes with six independent elements [e.g., *Gilbert*, 1971]. It is most applicable when the earthquake dimension and duration are smaller than the wavelengths and period of the seismic waves considered [*Dziewoński et al.*, 1981; *Ekström et al.*, 2012]. In this parameterization, the ground movement (e.g., velocity) is linearly linked to the six moment tensor components by Green's functions. Due to the nature of the long-period and long-wavelength seismic waves used for inversion, the MT solutions, including the time and location, are averaged descriptions of earthquakes. This is termed the centroid moment tensor (CMT) and is often generalized to include a source duration as well as the centroid time [*Dziewoński et al.*, 1981; *Ekström et al.*, 2012]. When an earthquake ruptures a very large area or is composed of a series of subevents, multiple source points with independent CMTs can be used to model the observations [e.g., *Tsai et al.*, 2005; *Li et al.*, 2009; *Duputel et al.*, 2012; *Nealy and Hayes*, 2015].

As discussed in section 1, a single CMT is insufficient to represent the Tonga-Samoa earthquake. Consequently, we experiment with using two separate CMTs to model the data, which consist of the first 5400 s of long-period vertical and transverse-component records, sampled at 10 s per sample (Figure S2). Green's functions are calculated with normal modes [*Masters and Widmer*, 1995] and the preliminary reference Earth model (PREM) [*Dziewoński and Anderson*, 1981]. We apply a grid search approach to explore the model space of potential source locations, durations, and initiation times. For every source combination, two CMTs are inverted and the waveform misfit is recorded, assuming no isotropic source components. Because shallow source depths are poorly resolved with long-period data, source depths are set to the GCMT depth of 12 km and only lateral locations are grid searched over 30 km spaced grids within −173.9° and −171.6° in longitude and −14.2° and −16.3° in latitude (Figure S2). Source durations are grid searched from 30 to 160 s for the first source and 40 to 160 s for the second one, assuming a symmetric triangular source-time function, and initiation times are grid searched from 0 to 30 s for the first source and from 40 to 100 s for the second source. Since only a small decrease in the overall data misfit can be achieved with more than two point sources, we restrict our analysis to two CMTs.

3. Results

Integrated back-projection images over the ∼160 s duration of the earthquake show clear frequency-dependent rupture behavior (Figure 2). The LF back-projection shows two distinct rupture zones, one large energy burst locating northwest of the epicenter east of the trench and another strong energy burst occurring landwardly west of the trench. If the landward rupture happened at the subduction interface, the LF energy burst within the subduction zone does not extend deeper than ∼40 km [*Hayes et al.*, 2012]. On the other hand, most of the radiated energy appears in the seaward region of the trench axis for HF back-projection. The bulk of the HF energy was released northwest of the epicenter, and there is not much HF energy release imaged west of the trench axis. Besides the large energy concentration northwest of the epicenter location, two noticeable radiation sources are seen southeast of the epicenter in the integrated HF image (Figure 2).

More rupture propagation details can be inferred from the stacked source-time functions (SSTF) and the snapshots (Figure 2). Compared to the LF stacked source-time function, two strong HF energy episodes were released from 0 to 20 s and from 60 to 80 s. Two energy episodes, 80 to 100 s and 120 to 140 s, are discernible in the low-frequency SSTF. The normalized LF integrated-power images (normalized with the maximum power within each 20 s window) reveal rupture around the epicenter for the first 20 s, a northwestward rupture followed by an apparent westward rupture across the trench axis from 20 to 40 s, a southeastward rupture in the seaward region from 40 to 80 s, and a southward rupture in the subduction zone from 40 to 60 s. Bilateral seaward rupture is also observed in the normalized HF integrated-power images. The apparent westward rupture across the trench axis is also imaged by the HF back-projection from 20 to 40 s. The southward rupture along the subduction interface (40 to 60 s) does not radiate much high-frequency energy. A coherent seismic radiator is imaged by both LF and HF back-projections from 80 to 100 s northwest of the epicenter, which is landward and spatially close to the westward rupture episode crossing the trench axis from 20 to 40 s. Another coherent radiator is located southwest of the epicenter west of the trench axis from 120 to 160 s, corresponding to the discernible energy episode in the low-frequency SSTF. The radiator is also visible in HF back-projection images but is less coherent.

The overall rupture process is summarized in Figure 3 and characterized by different rupture strands, which we term Branches. Bilateral rupture occurred in the seaward wall of the trench, northwestward for the first

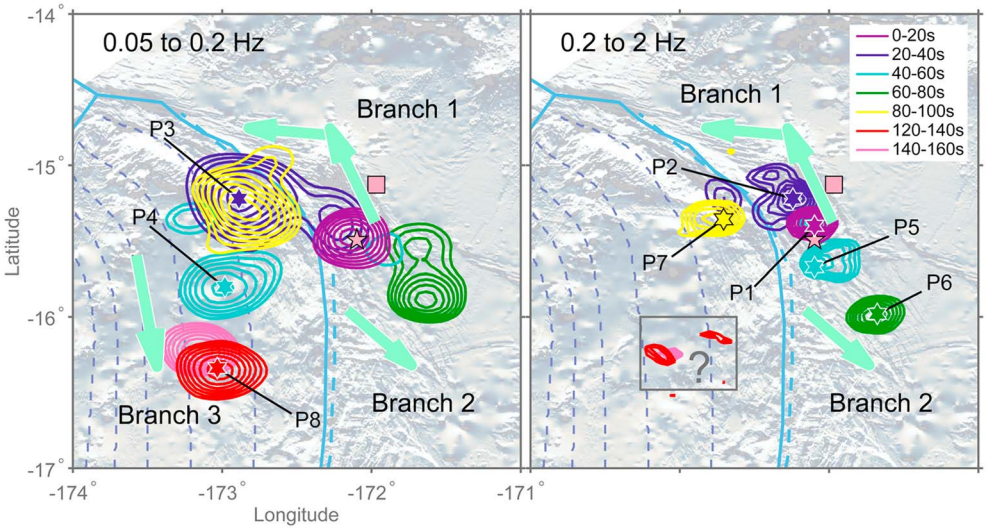

Figure 3. Rupture evolution of the 2009 Tonga-Samoa earthquake as inferred from back-projection. (left) Low frequency (LF); (right) high frequency (HF). Apparent energy burst peaks are labeled as P1 to P8.

40 s (Branch 1) and southeastward from 40 to 80 s (Branch 2). From ~27 to 60 s (Figure S3), Branch 3 of the earthquake broke the subduction interface and ruptured from north to south no deeper than ~40 km (Slab 1.0 inferred depth [*Hayes et al.*, 2012]). The peak locations of the energy bursts are denoted as P1 to P5 for the first 60 s (Figure 3). Energy bursts P6 to P8 occurred within 2 min of the earthquake initiation and are possible triggered early aftershocks (Figure 3). As part of Branch 2, the energy burst from 60 to 80 s (P6) is identified as a reverse-faulting early aftershock, since the *P* wave polarities of pulses associated with P6 are opposite to the other energy bursts east of the trench (P1, P2, and P5, Figure 4). The coherent seismic radiators, 80 to 100 s (P7) and 120 to 140 s (P8) may reflect the last stage of Branch 3 rupture, lasting until 160 s. Alternatively, they may also be very early aftershocks triggered by the earlier rupture. In either case, Branch 3 rupture experienced more than one rupture episode. For comparison, the *Lay et al.* [2010] array back-projection results indicated possible subevents around 52 s and 91 s, which are probably Branch 3 in Figures 2 and 3. They also observed an early aftershock occurring around 118 s, which might correspond to P8 (Figure 3).

Additional evidences for the energy bursts, aftershocks, and their focal mechanisms are provided by aligned seismograms and *P* wave polarities of the associated pulses. The LF velocity seismograms are aligned by azimuth in Figure 4. Each trace is normalized in two time windows separately (0 to 30 s and 20 to 160 s) to enhance the weak signals in the first 30 s. Using the locations of the energy bursts from Figure 3, we then try to find the best rupture time to explain the coherent pulses for all the azimuths. The theoretical arrivals (IASP91) [*Kennett and Engdahl*, 1991] of the inferred source and aftershock locations are shown as colored bands in Figure 4. The eight energy bursts can explain the pulses in the traces at most azimuths. Pulses associated with P1, P2, and P5 share coherent negative polarities, confirming the normal-faulting focal mechanism of the Branch 1 and Branch 2 ruptures. In contrast, pulses associated with P3 and P4 share coherent positive polarities, supporting the reverse-faulting focal mechanism of the Branch 3 rupture. Positive polarities of the pulses associated with P6, P7, and P8 suggest reverse-faulting focal mechanisms. Because of the different focal mechanisms of P5 and P6, the Branch 2 rupture is unlikely to involve continuous rupture from 40 to 80 s and may have had one southward rupture segment (P5, 40 to 60 s), which triggered an aftershock on an adjacent fault (P6, 60 to 80 s). The observed coherent positive polarities for the later events are unlikely to be the *sP* phases, as a polarity shift is expected in North American stations (azimuth 0° to 60°), if the pulses were *sP* instead of direct *P* waves (Figure S4). They are also unlikely to be the *pP* phases, as there are no identifiable *P* phases proceeding the observed coherent phases, which should arrive ~6 s ahead of *pP* phases (Figure S4).

To further verify the existence of P6 to P8, we filtered 935 globally recorded *P* waves into two frequency bands (0.5 to 2 Hz and 1 to 5 Hz) and then stacked the envelope functions of the records (Figure 5) using the approach of *Fan and Shearer* [2016]. For each target energy burst or possible early aftershock location (P1 to P8), the envelope functions are time shifted using the predicted arrivals of the burst location before stacking to account for arrival-time differences due to different source locations. The stacked function is then

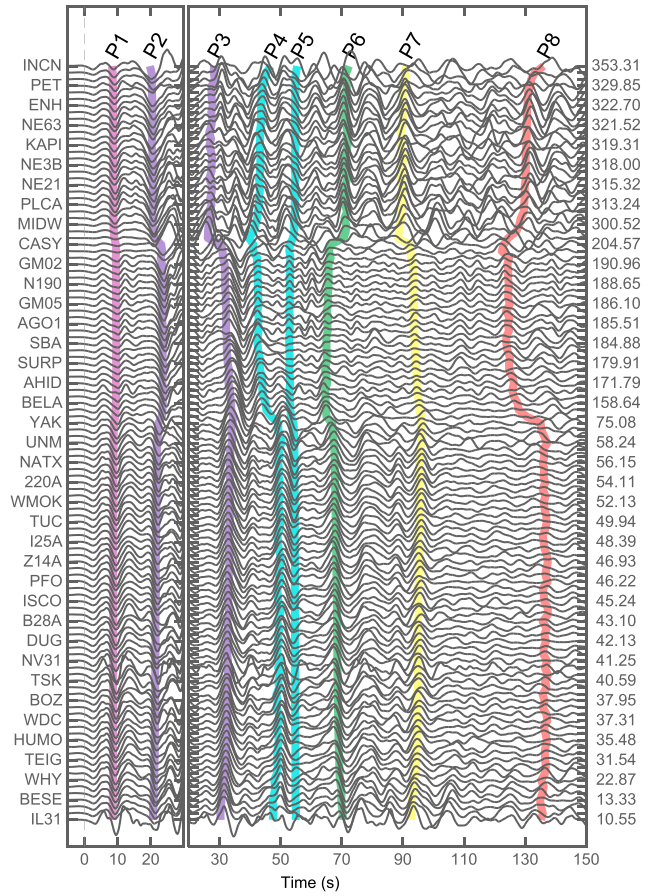

Figure 4. Aligned velocity seismograms (low-frequency, 0.05–0.2 Hz) with predicted traveltime arrivals of the observed energy busts in Figure 3. The records are sorted by azimuth, as listed on the right side of every third station with corresponding station names listed on the left side. Inferred rupture times of P1 to P5 are 9 s, 22 s, 31 s, 45 s, and 54 s. Inferred rupture times for P6 to P8 are 68 s, 93 s, and 130 s.

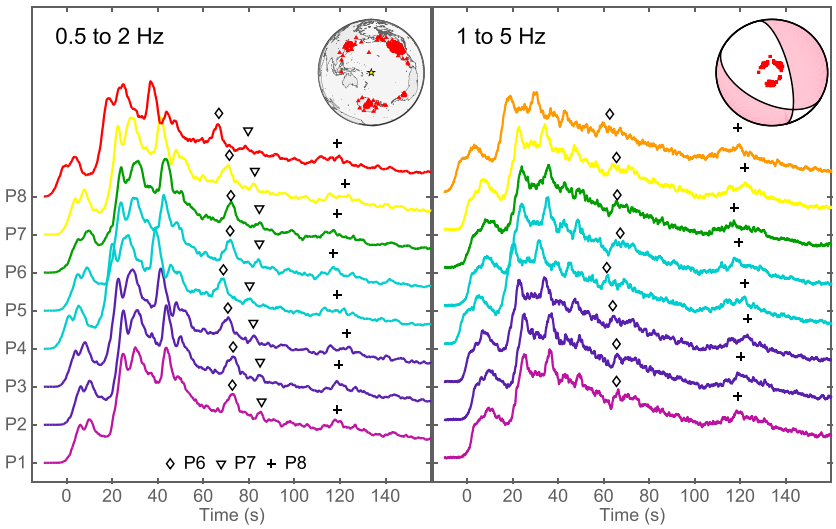

Figure 5. (right) Stacked envelope functions (0.5 to 2 Hz) of energy bursts P1 to P8, with station map plotted as upper right corner insert. (left) Stacked envelope functions (1 to 5 Hz) of energy busts P1 to P8, with station polarities on the lower hemisphere as upper right corner insert (red, negative). There are 935 stations used for stacking. The envelope functions are calculated with a standard Hilbert transform without smoothing.

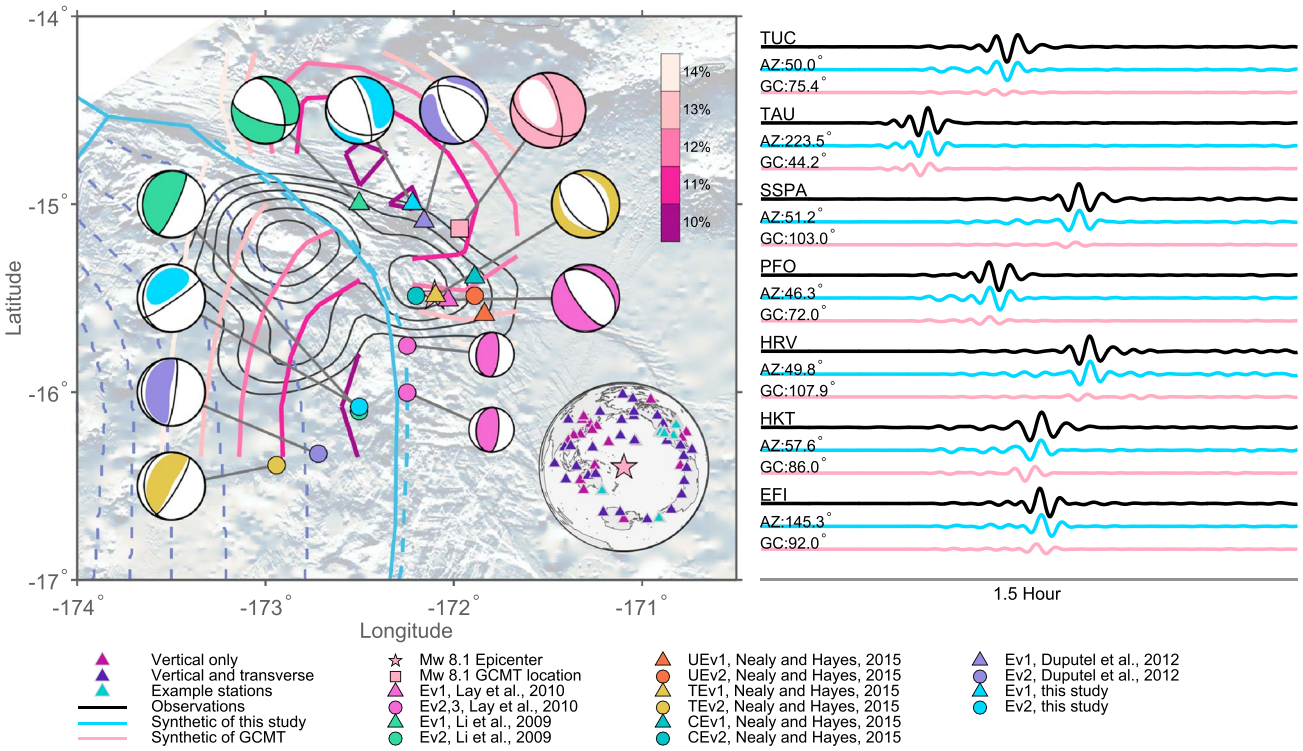

Figure 6. Comparison of multiple moment tensor solutions with other available source models. (left) Multiple moment tensor solutions (beach balls), misfit contours for our two-CMT solution (colored lines), and integrated LF back-projection results (gray contours). Focal mechanisms are from *Ekström et al.* [2012], *Lay et al.* [2010], *Li et al.* [2009], *Duputel et al.* [2012], *Nealy and Hayes* [2015], and this study. For solutions of *Nealy and Hayes* [2015], UEv1 and UEv2 are unconstrained solutions from grid searching the centroids, TEv1 and TEv2 are solutions constraining the second subevent to be landward of the trench while grid searching the other centroids, and CEv1 and CEv2 are solutions matching the time delays and depths as *Lay et al.* [2010] while grid searching the other centroids. Stations used for our multiple moment tensor solution are mapped in the lower right corner of Figure 6 (left). For blue and teal colored stations, both vertical and transverse recordings are used; for purple stations, only vertical recordings are used. (right) The transverse-component data fit for the teal stations. AZ and GC stand for azimuth and great circle distance.

normalized with the station number. From the stacks in both frequency bands, the majority of the quake energy was released before 60 s. Clear pulses of P6 to P8 can be identified in the 0.5 to 2 Hz stacked envelope functions (Figure 5). *P* wave coda decay dominates the 1 to 5 Hz stacks, yet P6 and P8 can be easily identified.

Figure 6 shows results from our double CMT inversion to model the very long period data (200 to 500 s), compared to previously published source models. We performed a grid search in the seaward region east of the trench for the first subevent location and in the landward region west of the trench for the second subevent location (Figure S2). Our best fitting solution for the first subevent is located ~50 km north of the epicenter with centroid time and duration of 35 s and 70 s, respectively. The first subevent shares similar fault geometries with the GCMT solution with strike 344°, dip 72° to the east, and rake −68°. The estimated moment magnitude is M_w 8.0 for the first subevent. The second subevent locates on the shallow megathrust ~ 80 km southwest of the epicenter with moment magnitude M_w 8.1. The second subevent initiated 80 s after the first subevent and ruptured for about 80 s. The centroid time (~ 120s) and the focal mechanism of the second subevent are consistent with other two-point-source solutions [*Li et al.*, 2009; *Duputel et al.*, 2012; *Nealy and Hayes*, 2015]. With strike 183°, dip 15° to the east, and rake 40°, the second subevent fault geometry corresponds well to the subduction interface. Transverse records in the North American region require the second source to explain the waveforms (Figures 6 and S6), while the vertical records are insensitive to the existence of the second source (Figures S6 and S7). For comparison, published CMT solutions are listed in Table 1.

In *Lay et al.* [2010], the source model of the 2009 Tonga-Samoa earthquake consists of a M_w 8.1 normal-faulting main shock and two M_w 7.8 reverse-faulting subevents (Figure 6 and Table 1), rupturing from ~49–89 s and ~90–130 s, respectively. Together, the moment of these two M_w 7.8 subevents totals to a M_w 8.0 earthquake. The two triggered reverse-faulting subevents likely correspond to the observed Branch 3 in Figure 3. The

Table 1. Comparison of Available CMT Solutions

	Latitude (deg)/Longitude (deg)/ Depth (km)	Strike (deg)/Dip (deg)/ Rake (deg)	Centroid Time (s)	Duration (s)	CLVD (ϵ)[a]	M_w
GCMT	−15.13/−171.97/12.0	346/62/−63	42.6	26.8	0.16	8.1
Li et al. [2009], Ev1	−15.00/−172.50/12.0	340.7/45.4/−46.3	39.0	46.6		8.0
Li et al. [2009], Ev2	−16.1/−172.5/10.0	183.7/13.9/69.3	117.0	50.8		8.1
Lay et al. [2010], Ev1	−15.51/−172.03/18	152/67/−77	33	60		8.1
Lay et al. [2010], Ev2	−16.01/−172.43/18	185/29/90	69	40		7.8
Lay et al. [2010], Ev3	−16.01/−172.43/18	185/29/90	110	40		7.8
Duputel et al. [2012], Ev1	−15.09/−172.16/15.5	157/64/−70	59.2	53.6	−0.07	8.03
Duputel et al. [2012], Ev2	−16.33/−172.72/15.5	176.9/10.9/79.4	125.4	40	−0.006	8.05
Nealy and Hayes [2015] , FEv1	−15.19/172.20/15.5	349.9/45.9/−84.6	66	66		8.22
Nealy and Hayes [2015] , FEv2	−15.19/172.20/15.5	158.1/39.6/51.7	85	80		8.16
Nealy and Hayes [2015] , UEv1	−15.59/−171.84/30.5	356.0/40.1/−78.5	66	66		8.23
Nealy and Hayes [2015] , UEv2	−15.49/−171.89/23.5	162.4/47.1/57.9	85	80		8.17
Nealy and Hayes [2015] , TEv1	−15.49/−172.10/17.5	330/44/−81	50	50		8.0
Nealy and Hayes [2015] , TEv2	−16.39/−172.94/17.5	178.5/18/59	182	182		8.07
Nealy and Hayes [2015] , CEv1	−15.39/−171.88/17.5	153.0/61.5/−81.6	50	50		8.03
Nealy and Hayes [2015] , CEv2	−15.49/−172.20/17.5	171.3/23.5/51.1	182	182		8.02
This study, Ev1	−15.00/−172.22/12.0	344/72/−68	35	70	-0.05	8.0
This study, Ev2	−16.08/−172.50/12.0	183/15/40	120	80	−0.20	8.1

[a]Compensated linear vector dipole (CLVD) is measured with $\epsilon = \sigma_2 / \max(|\sigma_1|, |\sigma_3|)$. For solutions of *Nealy and Hayes* [2015], FEv1 and FEv2 are solutions with one fixed centroid location, UEv1 and UEv2 are unconstrained solutions with grid searching the centroids, TEv1 and TEv2 are solutions constraining the second subevent to be landward of the trench while grid searching the other centroids, and CEv1 and CEv2 are solutions matching the time delays and depths as *Lay et al.* [2010] while grid searching the other centroids. The first subevent is dipping to the east when the strike is ∼344° or is dipping to the west when strike is ∼153°.

locations of the subevents in *Lay et al.* [2010] are offset from our best fitting CMT solutions, with the initial normal-faulting event located southeast of our corresponding CMT (and south of the GCMT) and the later two events located east and northeast of our second event (Figure 6). In *Duputel et al.* [2012], the source model consists of a M_w 8.03 normal-faulting main shock and a M_w 8.05 reverse-faulting subevent (Table 1). The time delays of the two subevents are 32.4 s and 105.4 s, with durations 53.6 s and 40 s, respectively. The two subevents of *Duputel et al.* [2012] are located close to our subevents with depths of 15.5 km. *Nealy and Hayes* [2015] experimented with fixing the centroid locations of the two subevents, grid searching the centroids, constraining the second subevent to be west of the trench while grid searching the other centroids, and matching the time delays and depths of *Lay et al.* [2010] while grid searching the other centroids (Figure 6 and Table 1). They found that the constraints do not notably influence the results, which suggests that the spatial and temporal resolution of the very long period data are limited, while the resolved focal mechanisms are robust. Their two-point-source solution (constraining the second subevent to be west of the trench) is consistent with a M_w 8.0 normal-faulting subevent and a M_w 8.07 reverse-faulting subevent (Table 1). The time delays of the two subevents are 25 s and 91 s, with durations 50 s and 182 s respectively. The first subevent of *Nealy and Hayes* [2015] is located at the epicenter, and the second subevent ∼50 km southeast of our solution, with a depth of 17.5 km. The focal mechanisms of these studies [*Lay et al.*, 2010; *Duputel et al.*, 2012; *Nealy and Hayes*, 2015] are in rough agreement with our results. As discussed below, the differences in the CMT solutions among these studies are likely within the range of uncertainty of multiple CMT solutions for this complicated earthquake. We prefer our solution because its reverse-faulting event is more clearly westward of the trench and closer to the long-period energy imaged by the LF back-projection.

4. Resolution and Uncertainties

There are intrinsic ambiguities in back-projection and CMT analysis. The back-projection relies on the reference hypocenter location, which is based on body wave observations. The centroid locations resolved in CMT analysis are mainly based on the surface wave and *W* phase observations. Before drawing conclusions about the rupture process, it is important to understand the resolution and uncertainties of the back-projection

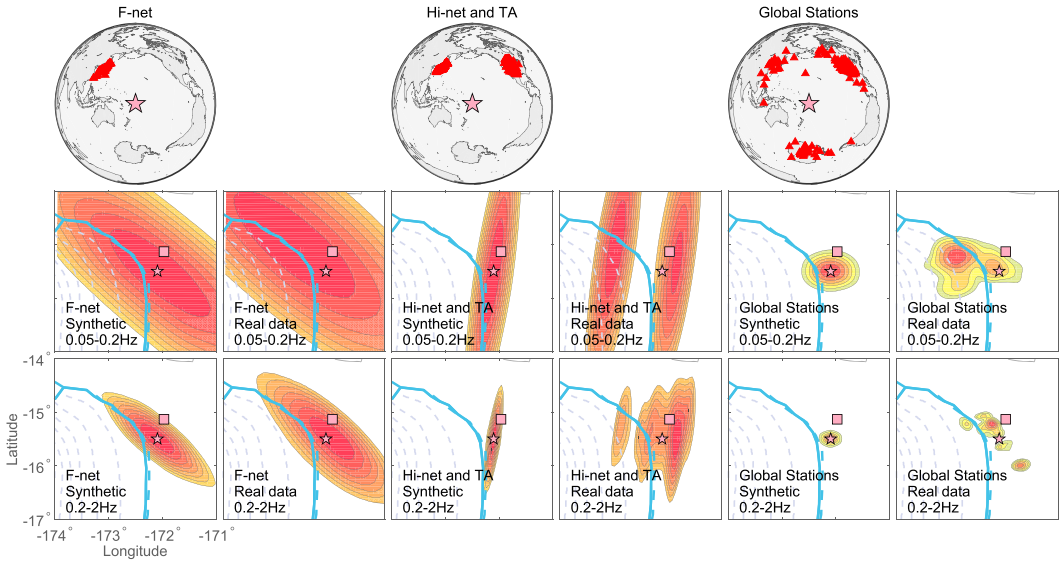

Figure 7. Comparison of theoretical resolving power and time-integrated back-projection results from two frequency bands ((top) LF; (bottom) HF) for the Tonga-Samoa earthquake obtained from F-net, a combined array (Hi-net and TA), and the global stations.

images. To do this, we have performed five different types of tests. First, for any given station set, the theoretical resolution can be computed from the station distribution and the data bandwidth by randomly assigning a single representative recorded *P* wave train to all the stations, then back-projecting these traces. This provides an estimate of the resolution of the station distribution given the frequency content of the data (Figure 7). As expected, the spatial resolution is proportional to the bandwidth used for back-projection with the same network. The theoretical spatial resolution of the LF/HF data is roughly circular and about 50 km/25 km in radius, a result of the good azimuthal coverage of the globally located stations.

Another way to assess the robustness of the observed features is to perform back-projection with a spatial subset of the network. Robust features observed with the global network are expected to also appear in regional array data results, albeit at lower resolution. To compare with *Lay et al.* [2010] and *Kiser and Ishii* [2012] as well as our own results, we separately used F-net, Hi-net [e.g., *Okada et al.*, 2004; *Obara et al.*, 2005], and USArray (www.usarray.org) to image the Tonga-Samoa earthquake (Figure 7), using the same approach we used for the global data. In Figure 7, the theoretical resolution for F-net is too limited to distinguish potential multiple subevents. The results from F-net mainly show a concentration of the energy release northwest of the epicenter. Combining multiple arrays can improve the resolution, but distortions are still present. To combine Hi-net high-sensitivity records and USArray (TA) broadband records, we first use a time domain recursive filter to convert the Hi-net recordings to broadband recordings before the alignment [*Maeda et al.*, 2011]. Because 1 – 5 Hz *P* waves were used to image the rupture process, Branch 3 rupture was not resolved in *Kiser and Ishii* [2012]. However, as shown in Figure 7, the LF energy release within the subduction zone is also imaged with Hi-net and USArray. For the dense arrays, F-net, Hi-net, and USArray, each trace is inversely weighted by the number of contributing stations within 1°. This weighting scheme is adopted so that we could have a fair comparison of the back-projection results. Other sophisticated weighting strategies might improve the resolution when considering array geometry, epicentral distances, and data quality.

To assess potential biases introduced by the complexities of the wavefield and the path effects, the resolution can be determined by performing back-projection on smaller events within the same region with similar station coverage as the main shock. The resolution for the main shock should be at least as good as that seen in the smaller event images, since smaller events may themselves have ruptured extended areas and usually have lower signal-noise-ratios for *P* waves and fewer usable stations. We performed back-projection on four nearby $M_w \geq 6$ earthquakes (Figure 8). The images of the smaller earthquakes span a similar spatial extent as that seen in the theoretical resolution tests for LF data (Figures 7 and 8) and are free of obvious artifacts. From Figure 8, the back-projection images of the smaller earthquakes are comparable to or smaller than the major

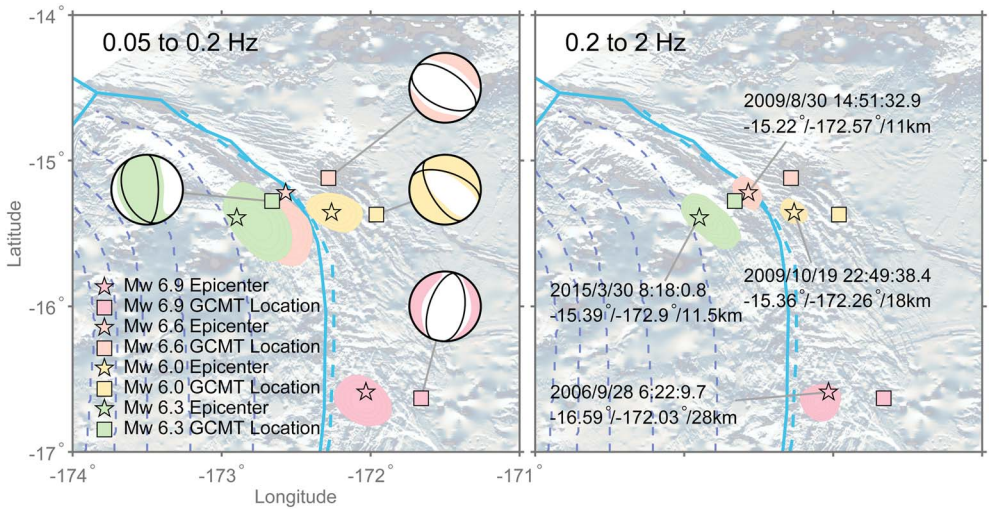

Figure 8. Time-integrated back-projection images of four ~*M*6 earthquakes in the region. Three normal-faulting earthquakes are in the seaward region, and one reverse-faulting earthquake in the landward region. The M_w 6.6, 30 August 2009 foreshock occurred on a possible linking fault that connects the seaward faults with the megathrust. The M_w 6.0, 19 October 2009 aftershock occurred on the same fault as the main shock.

energy bursts seen in Figure 3, showing that the three main shock rupture stages and three early aftershocks are clearly resolved.

Finally, we attempt with two more tests to assess the quality of the back-projection when there are multiple subvents in different locations with different mechanisms. In particular, for the 2009 Tonga-Samoa earthquake, the complex structure of the region might cause rapid Green's function variations near the subduction zone. For an extended rupture, the empirical time corrections based on the initial rupture near the hypocenter might not be appropriate for the later stages of the earthquake, where *P* polarity flips due to mechanism changes might also be present. Under some conditions, these problems could shift the rupture to erroneous locations/time or cause artifacts in the back-projection images. To address the problem, we performed back-projection of the four *M*6 earthquakes with time shifts and weighting factors obtained from main shock waveform alignment (Figure 9). For any of the *M*6 earthquakes, only stations that recorded both the main shock and the *M*6 earthquake are used, which results in fewer useable stations. The empirical corrections are derived from LF waveform cross correlations of the main shock records, and they are applied to obtain back-projection images of the *M*6 earthquakes at both frequency bands. The low-frequency back-projection results of all four *M*6 earthquakes are well resolved despite their different focal mechanisms and large spatial extents at all directions (Figure 9). The high-frequency back-projections are robustly resolved at the epicenters for all the *M*6 earthquakes except the 30 August 2009 foreshock, for which the peak energy location shifted ~25 km northeast of its epicenter (within the claimed uncertainties). The apparent shift could indicate a spatial bias of the HF back-projection when rupture occurs at the trench axis. However, because the other *M*6 earthquakes are well resolved at both sides of the trench axis, it is possible that the HF spatial drift of the foreshock indicates the termination stage of the earthquake, as it locates close to the edge of the LF image of the earthquake. All of the *M*6 earthquake back-projection images are well resolved, their extents are within our claimed uncertainties, and the results do not have obvious artifacts. This test strongly supports our observations of the main shock and shows the robustness of the imaged multiple branching rupture.

To further test the robustness of the back-projection images for the Tonga-Samoa event, we generate a "synthetic" data set by combining the recorded data from two local ~*M*6 events in the region, a normal-faulting seaward wall earthquake (M_w 6.0, 19 October 2009) and a thrust earthquake (M_w 6.3, 30 March 2015) on the subduction interface (Figure 10). These two events are close to the observed locations of energy bursts P1 and P3. We sum the first 100 s data from the two events, with a 20 s delay for the thrust event. The summation preserves possible multiples, reflections, and noise in the *P* waves of the first normal-faulting earthquake and carries them into the *P* waves of the second reverse-faulting earthquake. The realistic noise in conjunction with the rapid Green's function variation across the trench could introduce biases or artifacts to the images of the second event. We then back-project the synthetic data set of the composite events following the same

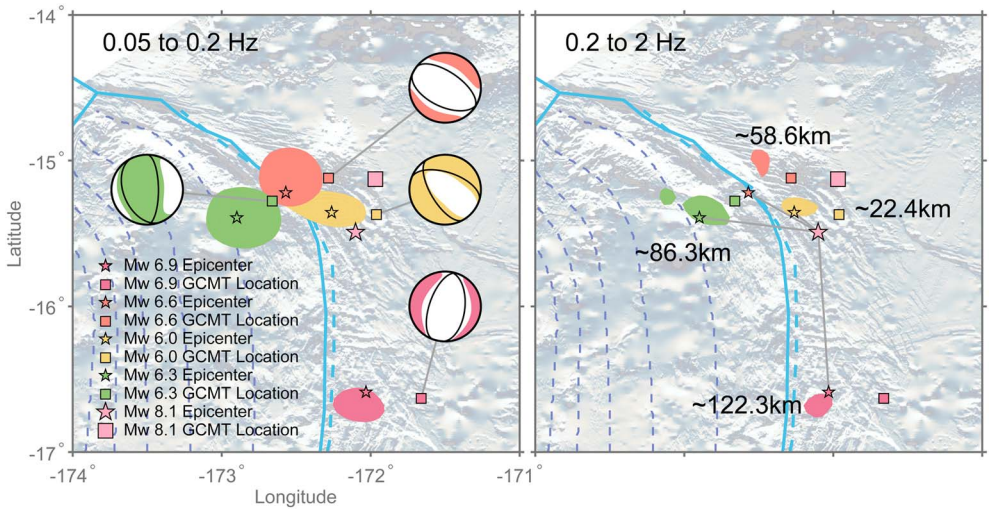

Figure 9. Time-integrated back-projection images of four ~*M*6 earthquakes in the region with waveform alignment derived from the main shock. The symbols are similar to Figure 8. The epicentral distances of the *M*6 earthquakes from the main shock are shown in Figure 9 (right).

procedure applied to the main shock, with the empirical time shifts, normalization factors, and weighting factors purely derived from the initiating normal-faulting earthquake (Figure 8). The results show that the second earthquake can be well resolved both spatially and temporally, even though the waveform alignment, normalization, and weighting factors are based entirely on the first earthquake (Figure 10). No significant artifacts or biases are observed in the images, such as ghost ruptures offset from the main rupture patches. The results show that LF back-projection works better than HF back-projection for this case, indicating that the 3-D Green's functions do not bias the LF results very much, the opposite of the expected strong influence due to the complex local velocity variations. This empirical calibration test supports the validity of the observed Branch 3 rupture of the megathrust interface.

By using a globally distributed network, artifacts in back-projection images can be greatly reduced. As shown in Figures 7–10, the good azimuthal coverage of the global station network minimizes the "swimming" artifacts [e.g., *Xu et al.*, 2009; *Koper et al.*, 2012; *Meng et al.*, 2012] that are troublesome in back-projection images from regional arrays. For large shallow earthquakes, depth phases cannot easily be separated from the direct phases and usually interfere with the ensuing *P* waves that are associated with later parts of the rupture. However, as shown in *Fan and Shearer* [2015], the depth phases and other complexities do not bias the back-projection results very much when full azimuthal station coverage is available.

Our best fitting single moment tensor solution has 18% RMS data misfit, while the best two-source solution has 9.5% misfit. The significant misfit reduction strongly suggests the necessity of a second reverse-faulting subevent to accompany the initial normal-faulting event. Our preferred reverse-faulting subevent shares similar strikes and dips with other studies [*Li et al.*, 2009; *Lay et al.*, 2010; *Duputel et al.*, 2012; *Nealy and Hayes*, 2015]. But the rake varies from solution to solution for all the models (Table 1). This variation might reflect differences in the data set and/or inversion procedure. Our solution is mainly constrained by the far-field surface waves, while other studies implemented near-field observations. Off-diagonal elements of the moment tensor solutions are poorly resolved for shallow earthquakes. Therefore, different inversion procedures with various approaches may give different values, which will lead to different rake values. Even though all the currently available CMT solutions share similar focal mechanisms, the large variations in their locations and times imply poor spatiotemporal constraints on the two subevents (Figures 6 and S8). The very long period data and Green's functions calculated from a 1-D velocity model are potential causes for some of the variation since the GCMT solution was obtained using 3-D velocity corrections. For our two-point-source solution, the misfit contours shown in Figure 6 represent the uncertainties of a subevent location when the other subevent is fixed at the labeled preferred location. When moving the second subevent to the locations in *Duputel et al.* [2012] and *Nealy and Hayes* [2015], the overall misfit increases to 10%–11%. The very long period data have poor temporal resolution for both subevent durations and centroid times (Figure S8). The second subevent centroid time can vary from 90 to 130 s, with total data misfit less than 10%. Within a misfit of 10%, the sec-

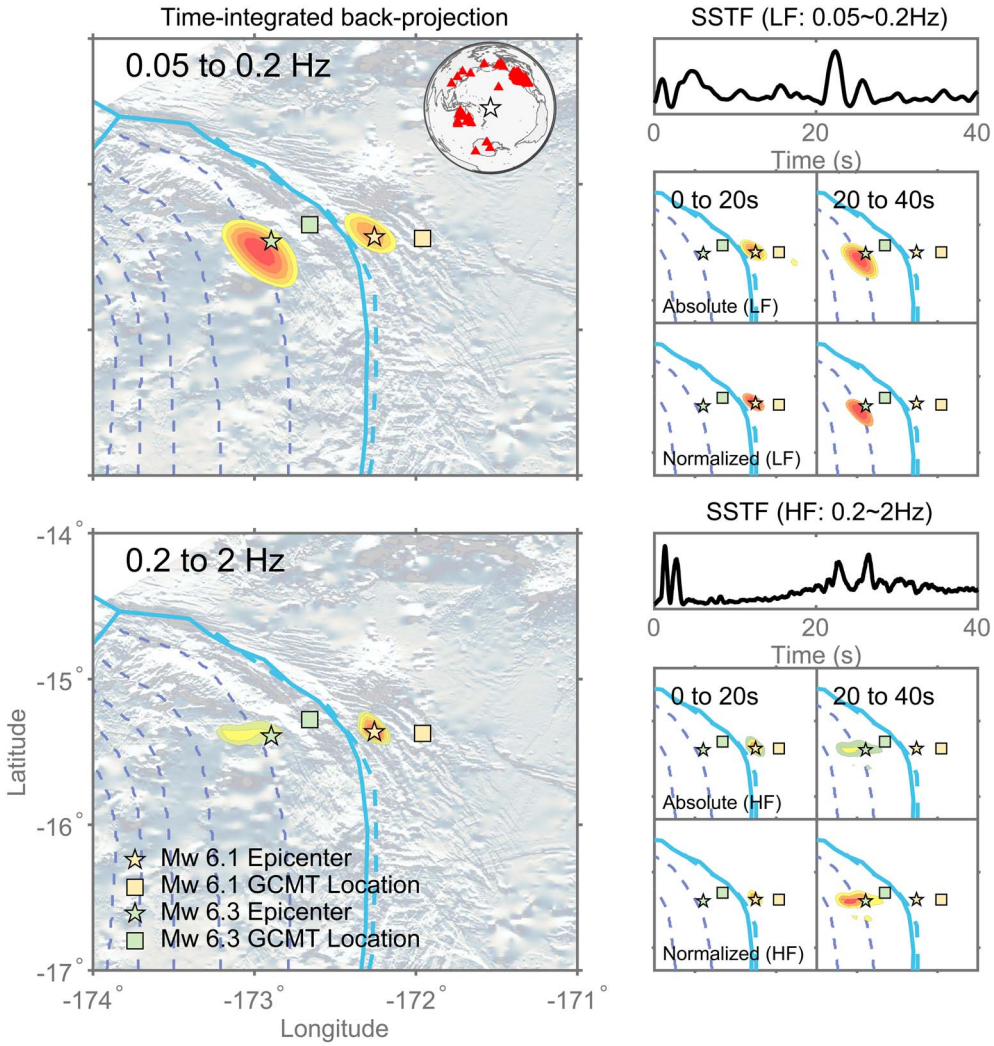

Figure 10. Back-projection results for a simulated multievent rupture, created by summing records from the normal-faulting seaward wall aftershock (M_w 6.0, 19 October 2009) and the thrust earthquake (M_w 6.3, 30 March 2015) on the subduction interface. (top row) Low-frequency (LF, 0.05–0.2 Hz) time-integrated back-projection image, stacked source-time function (SSTF), and time snapshots; (bottom row) high-frequency (HF, 0.2–2 Hz) time-integrated back-projection image, stacked source-time function, and time snapshots. Stations used for the back-projection analysis are mapped in the upper right corner of the integrated LF back-projection image. Because of the magnitude difference and different frequency content, we increase the recording amplitudes four times for the normal-faulting aftershock at LF and increase the recording amplitudes twice for the reverse-faulting earthquake at HF. Absolute and Normalized represent the power of each window normalized with the maximum power within 160 s and each 20 s window, respectively.

ond subevent duration can vary from 40 to 100 s, and the first subevent can vary from 50 to 90 s. These small changes in misfit for large shifts in the CMT centroids probably is due to the fact that only stations in North America strongly require the second source, and without good azimuthal coverage its location is not well constrained. The reverse-faulting subevent only contributes dominantly to the transverse component at certain azimuths, as shown by the theoretical radiation patterns (Figure S9).

The preferred CMT centroid location of the reverse-faulting subevent is ~100 km southeast of the landward peak energy burst observed with back-projection, and the initiation time is ~50 s later (Figures 2, 3, 6, and S3). The imaged P8 is spatiotemporally close to the second subevent, but its relative power is much weaker than P3 and P4. Given these differences, it is unlikely that back-projection is imaging the main moment release patch of the reverse-faulting subevent. This is not surprising, given that we filter the data to 0.002–0.005 Hz (200–500 s) to determine the CMT solutions while the "low-frequency" back-projection uses *P* waves filtered

at 0.05–0.2 Hz (5–20 s) and frequency-dependent rupture behavior has been observed in large earthquakes along major plate boundaries [e.g., *Lay et al.*, 2012; *Yao et al.*, 2013; *Meng et al.*, 2014; *Wang and Mori*, 2011b]. Our results are consistent with a scenario in which the reverse-faulting event initiated with a burst of 5–20 s energy seen in the back-projection and then ruptured to the south into a large slip patch that is seen in the CMT solutions but did not radiate enough short-period energy to coherently appear in the back-projection. Caution is warranted, however, as there are substantial resolution issues for both solutions because of limitations in data coverage and model-dependent uncertainties introduced by unknown velocity structures. The reverse-faulting CMT subevent is mainly resolved by transverse components of five North American stations (Figure 6) within a narrow azimuthal bin. The back-projection resolution depends on the array geometry and locations (Figure 7). Strong near-source velocity heterogeneity associated with the subducting slab is not accounted for in our Green's functions and could bias both the CMT and back-projection solutions. Despite these uncertainties, both preferred models lead to the same conclusion that at least two large subevents are involved in the Tonga-Samoa earthquake, they ruptured sequentially with the reverse-faulting subevent following the normal-faulting subevent, and the reverse-faulting subevent occurred west of the trench axis but no deeper than 40 km.

5. Discussion

The majority of aftershocks occurred within the subduction zone (Figures 2 and 11). The first day of aftershocks spans the region where energy release is observed in the LF back-projection image, with a concentration around the peak energy burst (Figure 2). One month of aftershocks [*International Seismological Centre*, 2013] show a similar pattern Figure 11. Combined with the seismicity, a very shallow dipping nodal plane (184°, 16°, and 40°) of the reverse-faulting subevent in Figure 6 is preferred. A clear aftershock band within the subduction zone concentrates from 20 to 40 km, in contrast to the paucity of seaward wall aftershocks. The aftershocks of the second subevent are confined from −15.2° to −17° in latitude, indicating the rupture of the reverse-faulting subevent extended about 200 km. All of the CMT solutions locate the second reverse faulting event south of −16°S (Figure 6), whereas there is a large concentration of the aftershocks from −15.2°S to −16°S. This aftershock zone spatially correlates with the P3 and P4 rupture imaged in the low-frequency back-projection, supporting the existence of the northern part of the trench west rupture.

To constrain the geometry of faults formed seaward of the trench axis, we calculate residual bathymetry from the 15 arc sec SRTM15_PLUS bathymetry compilation [*Becker and Sandwell*, 2012; *Sandwell et al.*, 2014]. Residual bathymetry is calculated by regionally subtracting a spectral average of the trench-normal topography (Figure 11) [*Bassett and Watts*, 2015a, 2015b]. Spectral averaging has been shown to be an effective means of removing steep topographic gradients associated with ocean trenches and here reveals complex along-strike variations in the spacing and geometry of extensional bend faults. South of −16.5°, bend faults are approximately strike parallel (or N-S) and have a mean spacing of ∼20 km. North of −15.3°, in contrast, faults display a strike closer to E-W and have a mean spacing of ∼5 km. In the intermediary zone, bend faults strike NW-SE and have a mean spacing of ∼ 8 km. The transition between approximately trench-parallel to almost trench-normal fault geometries is well correlated with an anticlockwise curve in the geometry of the trench axis. The preexisting seafloor fabric strikes approximately E-W [*Billen and Stock*, 2000; *Downey et al.*, 2007] and observed along-strike variations in fault spacing and geometry are likely driven by changes in the obliquity of this fabric with respect to the trench axis and azimuth of plate bending. This hypothesis is consistent with global compilations showing that when the seafloor-fabric is oriented at angles $<\sim 30°$ to the trench, the fabric is reactivated during bending and no significant new sets of faults develop [*Masson*, 1991; *Ranero et al.*, 2005].

Of most significance to this study are clear spatial correlations observed between the location and geometry of energy bursts and fault traces (Figures 3 and 12). Branch 1 and Branch 2 of the Tonga-Samoa earthquake are characterized by bilateral rupture NW and SE of the epicenter, respectively. Energy bursts P1 and P2 are aligned with the NW-SE trend of bend faults, as are energy bursts P5 and the early aftershock P6 (Figures 3 and 12). Faults in the northern region of the fracture zone strike approximately E-W, which is also mirrored by the azimuth between energy bursts P2 and P3 (Figures 3 and 11). It is here that the Tonga-Samoa earthquake appeared to rupture across the trench axis, linking the seaward components of this earthquake (Branches 1 and 2) to Branch 3, which ruptured the megathrust in a southwesterly direction (Figures 3 and 12). We note that the southerly extent of LF back-projection imaged megathrust rupture is approximately coincident with the southern region of a fore-arc block characterized by positive residual bathymetric anomalies (Figure 12).

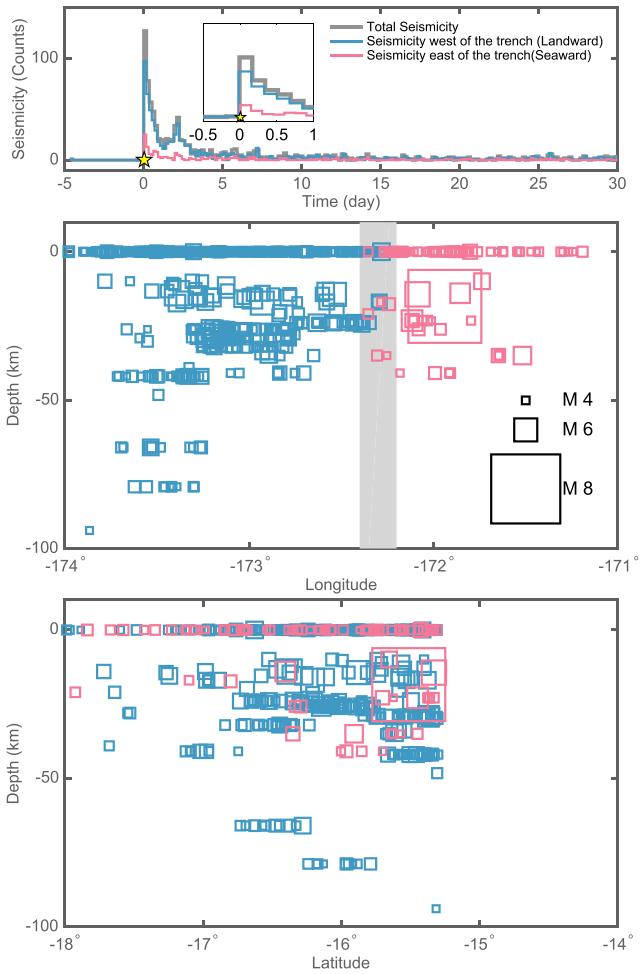

Figure 11. One month of aftershock activity of the 2009 Tonga-Samoa earthquake [*International Seismological Centre*, 2013]. Seismicity east of the trench is denoted with red, and the landward seismicity is shown in blue. (top) Event number versus time. (middle) Depth distribution along longitude; gray band shows the trench zone. (bottom) Depth distribution along latitude. Depths of events that cannot be vertically located are set to zero.

This suggests the fore arc (and hence megathrust) is segmented along strike, which may have limited the southerly extent of megathrust rupture (Stage 3) [*Bassett et al.*, 2016].

The back-projection images, along with the local bathymetry, provide a simple physical explanation for the rupture propagation and the anomalous nature of the 2009 Tonga-Samoa earthquake. We suggest that Branches 1 and 2 are natural consequences of the fault geometries, and the Branch 3 rupture is modulated by the structure and segmentation of the fore arc (Figures 2, 3, and 12). Between P2 and P3, there is an E-W trend fault that is partially subducted beneath the Tonga fore arc, which may link the seaward faults system with the megathrust. The M_w 6.6 foreshock (30 August 2009 Figure 8) that occurred 1 month before the main shock was probably on this or an adjacent linking fault, which is consistent with its normal-faulting mechanism. The change in the geometry of the trench axis enables reactivation of the seafloor fabric. The reactivated normal fault may have played a key role in facilitating the initiation of the Branch 3 rupture. If this holds true, the linking fault may promote both regions to rupture along a single earthquake, as observed for the Tonga-Samoa earthquake.

Although the different rupture branches of the 2009 Tonga-Samoa earthquake are robustly resolved in our back-projection images, the spatial resolution is too coarse to distinguish continuous rupture propagation from a series of triggered subvents for this complicated earthquake. In particular, the apparent trench-crossing rupture from 20 to 40 s observed by both LF and HF back-projection may be more favorably explained as a discontinuous jump across the trench via dynamic triggering (Figure 3). Either immediate triggering or con-

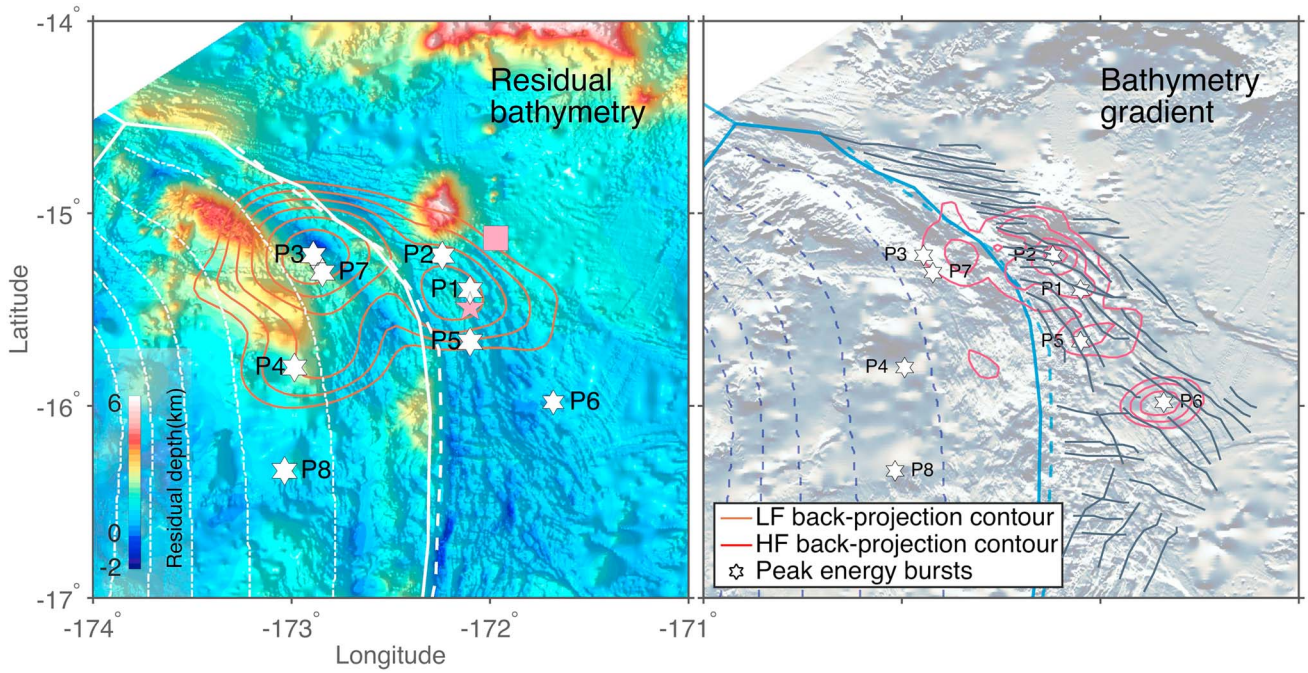

Figure 12. Ensemble of residual bathymetry and swath bathymetry from STRM 15 [*Becker and Sandwell*, 2012]. (left) Ensemble bathymetry. (right) Bathymetry gradient. Apparent energy burst (P1 – P8) locations are the same as those labeled in Figure 3. The integrated LF and HF back-projection results are shown in Figure 12 (left) and Figure 12 (right), respectively. Gray solid lines are inferred fault traces in the seaward wall of the trench.

tinuous rupture through a west-east normal linking fault could possibly initiate the Branch 3 rupture. The observed normal-reverse composite source model of the event connected via the linking fault could also be an early *M*8 reverse-faulting aftershock triggered simultaneously as the *M*8 normal-faulting earthquake propagates. With only estimates of average rupture velocities (~2 km/s, Figure S10), there is no clear distinction between multisubevent rupture and a main shock to very early aftershock rupture sequence. Therefore, we propose the second reverse-faulting subevent is triggered by the first normal-faulting subevent, with the possibility of continuous westward rupture from the east faults to the west faults of the trench. It makes sense to group subevents by how close they are in time and space, so we suggest that the apparent westward rupture from P2 to P3 as part of Branch 1 is a result of curved fault traces (Figure 11), assign the early aftershock P6 as part of Branch 2, as it is spatially and temporally close to P5 (Figure 3), and group P7 and P8 to Branch 3.

Frequency-dependent rupture behavior has been observed for large megathrust earthquakes and continental earthquakes [e.g., *Lay et al.*, 2012; *Yao et al.*, 2011; *Kiser and Ishii*, 2011; *Meng et al.*, 2011; *Koper et al.*, 2011; *Wang and Mori*, 2011a, 2011b; *Fan and Shearer*, 2015; *Grandin et al.*, 2015], and variations have been seen in both along-strike and dip directions [e.g., *Kiser and Ishii*, 2011; *Yao et al.*, 2013; *Meng et al.*, 2014; *Melgar et al.*, 2016]. The observed frequency-dependent variations could be expressions of depth-varying frictional properties [e.g., *Yao et al.*, 2013], multiple segmentation [e.g., *Yin and Yao*, 2016; *Denolle et al.*, 2015], different rupture properties over the fault plane [e.g., *Kiser and Ishii*, 2011], or different mechanisms [e.g., *Meng et al.*, 2014]. The frequency dependence of the Tonga-Samoa earthquake is different from these cases in the sense that the frequency-dependent rupture behavior is associated with different faults. The high-frequency deficient rupture at the megathrust interface and high-frequency enrichment at the seaward fracture zone is a pattern that is similar to that observed during the 2006 – 2007 Kuril Islands doublet [*Ammon et al.*, 2008; *Lay et al.*, 2009]. The significant difference in frequency content likely reflects the special faulting environments of the outer-rise/seaward wall faults and the subduction interface fault. Moreover, the clear along-strike separation of the LF back-projection energy bursts (P3 and P4) and CMT solution centroid of the Branch 3 rupture has not been observed in a single earthquake before, suggesting the complexities of the reverse-faulting earthquake, which itself may rupture more than one episode. The Branch 3 rupture for the Tonga-Samoa earthquake within the subduction zone is critical for the induced tsunami [*Zhou et al.*, 2012] (Figures 2 and 3), as very shallow megathrust ruptures with large vertical displacements can produce strong tsunamis, which often show little high frequency radiation [*Kanamori*, 1972].

The Tonga-Samoa earthquake represents an unusual normal-faulting/reverse-faulting doublet in which the thrust event occurred within 2 min of the initiating normal-faulting earthquake. This sequence is in the opposite order of the 2006–2007 Kuril Islands doublet, where a reverse-faulting main shock triggered a normal-faulting intraplate event 60 days later as a slab pulling effect. Other large trench-slope events preceding large interplate ruptures usually involve compressional, rather than extensional, faulting [*Christensen and Ruff*, 1988; *Lay et al.*, 1989]. The contrasting observations for the Tonga-Samoa earthquake show another possible scenario for great earthquakes at subduction zones when complex fault systems are present with reactivated preexisting seafloor fabrics. There is a possible partially subducted normal fault crossing the trench axis, which may link the seaward wall of the trench with the megathrust. If the linking fault can effectively transfer rupture from both sides, then this potential linkage would suggest a higher seismic risk for this region as ruptures could efficiently propagate from the seaward fault system to the megathrust and vice versa.

6. Conclusions

The 2009 Tonga-Samoa earthquake involved multiple ruptures on a system of faults, initiating as a normal-faulting earthquake located seaward of the trench axis that curved into the trench, triggering a reverse-faulting subduction thrust event dominated by long-period seismic radiation. As revealed by back-projection in different frequency bands, the spatiotemporal evolution of the earthquake can be characterized as a multibranch rupture process. Time-integrated back-projection images and snapshots show northwest rupture from 0 to 40 s (Branch 1), southeast rupture from 40 to 80 s (Branch 2), and southward rupture along the megathrust interface from ~30 to 160 s (Branch 3). Very early aftershocks (P6 to P8) are possibly triggered within 2 min located around the boundaries of the three rupture segments. The observed three-branch rupture is a natural consequence of the curved fault geometries associated with reactivation of preexisting fabric and fore-arc segmentation, which is illustrated by the collocation of observed energy bursts and bathymetrically inferred fault traces. Combined with a multiple moment tensor solution, the first two branches can be modeled as a M_w 8.0 bilateral normal-faulting earthquake and the last stage can be modeled with a M_w 8.1 reverse-faulting earthquake. The second reverse-faulting earthquake is triggered by the first normal-faulting earthquake, with possible involvement of a linking fault that is partially subducted into the megathrust interface, which may facilitate the initiation of the reverse-faulting subevent. One month of aftershocks indicate that the reverse-faulting event has a very shallow dip angle and extends about 200 km along strike and ruptured as north as −15.2°. The back-projection results show the frequency-dependent rupture pattern of the entire sequence, as the Branch 3 rupture of the reverse-faulting subevent is deficient in high frequencies. The rupture behaviors of the three branches reflect different faulting environments. The rupture pattern of the 2009 Tonga-Samoa earthquake reveals an interesting type of fault system involving seaward wall intraplate normal faults, megathrust reverse faults, and reactivated fabrics, which could possibly link faults at both sides of the trench and allow rupture sequentially across the trench. The special fault system geometry of the northern Tonga subduction zone poses a high seismic risk for that region as a potential host for great earthquakes and tsunamigenic earthquakes.

Acknowledgments

We thank Guy Masters and Zhitu Ma for providing normal mode data and programs for the Green's function calculation, Zhongwen Zhan and Soli Garcia for helpful discussions, and Jennifer Nealy and Zacharie Duputel for sharing their *W* phase CMT solutions. We thank the Editor, Yehuda Ben-Zion, the Associate Editor, and the anonymous reviewers for their helpful comments that improved the quality of the manuscript. The seismic data were provided by the Data Management Center (DMC) of the Incorporated Research Institutions for Seismology (IRIS) and National Research Institute for Earth Science Disaster Prevention in Japan (NIED). The earthquake catalog was downloaded from the International Seismological Center (ISC) and the Global Centroid Moment Tensor (GCMT) [*Ekström et al.*, 2012]. The bathymetry data were processed with the Generic Mapping Tools (GMT) [*Wessel and Smith*, 1991; *Wessel et al.*, 2013]. The data used in the study are publicly available at DMC (http://ds.iris.edu/ds/nodes/dmc/), and the processed data are available from the authors upon request. This work was supported by National Science Foundation grant EAR-1111111.

References

Ammon, C. J., H. Kanamori, and T. Lay (2008), A great earthquake doublet and seismic stress transfer cycle in the central Kuril Islands, *Nature*, *451*(7178), 561–565.

Bassett, D., and A. B. Watts (2015a), Gravity anomalies, crustal structure, and seismicity at subduction zones: 1. Seafloor roughness and subducting relief, *Geochem. Geophys. Geosyst.*, *16*(5), 1508–1540, doi:10.1002/2014GC005684.

Bassett, D., and A. B. Watts (2015b), Gravity anomalies, crustal structure, and seismicity at subduction zones: 2. Interrelationships between fore-arc structure and seismogenic behavior, *Geochem. Geophys. Geosyst.*, *16*(5), 1541–1576, doi:10.1002/2014GC005685.

Bassett, D., D. T. Sandwell, Y. Fialko, and A. B. Watts (2016), Upper–plate controls on co-seismic slip in the 2011 magnitude 9.0 Tohoku-oki earthquake, *Nature*, *531*, 92–96, doi:10.1038/nature16945.

Beavan, J., X. Wang, C. Holden, K. Wilson, W. Power, G. Prasetya, M. Bevis, and R. Kautoke (2010), Near-simultaneous great earthquakes at Tongan megathrust and outer rise in September 2009, *Nature*, *466*(7309), 959–963.

Becker, J., and D. Sandwell (2012), Development of Global Bathymetry and Topography at 15 arc seconds, *EOS Trans. AGU*, *1*, 0893.

Billen, M. I., and J. Stock (2000), Morphology and origin of the Osbourn Trough, *J. Geophys. Res.*, *105*(B6), 13,481–13,489, doi:10.1029/2000JB900035.

Bird, P. (2003), An updated digital model of plate boundaries, *Geochem. Geophys. Geosyst.*, *4*(3), 1027, doi:10.1029/2001GC000252.

Christensen, D. H., and L. J. Ruff (1988), Seismic coupling and outer rise earthquakes, *J. Geophys. Res.*, *93*(B11), 13,421–13,444, doi:10.1029/JB093iB11p13421.

Denolle, M. A., W. Fan, and P. M. Shearer (2015), Dynamics of the 2015 M7.8 Nepal earthquake, *Geophys. Res. Lett.*, *42*(18), 7467–7475, doi:10.1002/2015GL065336.

Downey, N. J., J. M. Stock, R. W. Clayton, and S. C. Cande (2007), History of the Cretaceous Osbourn spreading center, *J. Geophys. Res.*, *112*(B4), B04102, doi:10.1029/2006JB004550.

Duputel, Z., H. Kanamori, V. C. Tsai, L. Rivera, L. Meng, J.-P. Ampuero, and J. M. Stock (2012), The 2012 Sumatra great earthquake sequence, *Earth Planet. Sci. Lett.*, *351–352*, 247–257, doi:10.1016/j.epsl.2012.07.017.

Duputel, Z., L. Rivera, H. Kanamori, and G. Hayes (2012b), W phase source inversion for moderate to large earthquakes (1990–2010), *Geophys. J. Int.*, *189*(2), 1125–1147, doi:10.1111/j.1365-246X.2012.05419.x.

Dziewoński, A. M., and D. L. Anderson (1981), Preliminary reference Earth model, *Phys. Earth Planet. Inter.*, *25*(4), 297–356, doi:10.1016/0031-9201(81)90046-7.

Dziewoński, A. M., T.-A. Chou, and J. H. Woodhouse (1981), Determination of earthquake source parameters from waveform data for studies of global and regional seismicity, *J. Geophys. Res.*, *86*(B4), 2825–2852, doi:10.1029/JB086iB04p02825.

Ekström, G., M. Nettles, and A. Dziewoński (2012), The global CMT project 2004–2010: Centroid-moment tensors for 13,017 earthquakes, *Phys. Earth Planet. Inter.*, *200–201*, 1–9, doi:10.1016/j.pepi.2012.04.002.

Fan, W., and P. Shearer (2015), Detailed rupture imaging of the 25 April 2015 Nepal earthquake using teleseismic P waves, *Geophys. Res. Lett.*, *42*(14), 5744–5752, doi:10.1002/2015GL064587.

Fan, W., and P. M. Shearer (2016), Fault interactions and triggering during the 10 January 2012 M_w 7.2 Sumatra earthquake, *Geophys. Res. Lett.*, *43*, 1934–1942, doi:10.1002/2016GL067785.

Garcia, E. S., D. T. Sandwell, and W. H. Smith (2014), Retracking Cryosat-2, Envisat and Jason-1 radar altimetry waveforms for improved gravity field recovery, *Geophys. J. Int.*, *196*(3), 1402–1422, doi:10.1093/gji/ggt469.

Gilbert, F. (1971), Excitation of the normal modes of the Earth by earthquake sources, *Geophys. J. Int.*, *22*(2), 223–226, doi:10.1111/j.1365-246X.1971.tb03593.x.

Govers, R., and M. Wortel (2005), Lithosphere tearing at STEP faults: Response to edges of subduction zones, *Earth Planet. Sci. Lett.*, *236*(1–2), 505–523, doi:10.1016/j.epsl.2005.03.022.

Grandin, R., M. Vallée, C. Satriano, R. Lacassin, Y. Klinger, M. Simoes, and L. Bollinger (2015), Rupture process of the M_w = 7.9 2015 Gorkha earthquake (Nepal): Insights into Himalayan megathrust segmentation, *Geophys. Res. Lett.*, *42*(20), 8373–8382, doi:10.1002/2015GL066044.

Hayes, G. P. (2011), Rapid source characterization of the 2011 M_w 9.0 off the Pacific coast of Tohoku earthquake, *Earth, Planets, Space*, *63*(7), 529–534, doi:10.5047/eps.2011.05.012.

Hayes, G. P., P. S. Earle, H. M. Benz, D. J. Wald, R. W. Briggs, and USGS/NEIC Earthquake Response Team (2011), 88 hours: The U.S. Geological Survey National Earthquake Information Center response to the 11 March 2011 M_w 9.0 Tohoku earthquake, *Seismol. Res. Lett.*, *82*(4), 481–493, doi:10.1785/gssrl.82.4.481.

Hayes, G. P., D. J. Wald, and R. L. Johnson (2012), Slab1.0: A three-dimensional model of global subduction zone geometries, *J. Geophys. Res.*, *117*(B1), B01302, doi:10.1029/2011JB008524.

Houser, C., G. Masters, P. Shearer, and G. Laske (2008), Shear and compressional velocity models of the mantle from cluster analysis of long-period waveforms, *Geophys. J. Int.*, *174*(1), 195–212, doi:10.1111/j.1365-246X.2008.03763.x.

International Seismological Centre (2013), *On-Line Bulletin*, Int. Seis. Cent., Thatcham, U. K.

Ishii, M., P. M. Shearer, H. Houston, and J. E. Vidale (2005), Extent, duration and speed of the 2004 Sumatra-Andaman earthquake imaged by the Hi-net array, *Nature*, *435*(7044), 933–936.

Ji, C., D. J. Wald, and D. V. Helmberger (2002), Source description of the 1999 Hector mine, California, earthquake, Part II: Complexity of slip history, *Bull. Seismol. Soc. Am.*, *92*(4), 1208–1226, doi:10.1785/0120000917.

Kanamori, H. (1972), Mechanism of tsunami earthquakes, *Phys. Earth Planet. Inter.*, *6*(5), 346–359, doi:10.1016/0031-9201(72)90058-1.

Kennett, B. L. N., and E. R. Engdahl (1991), Traveltimes for global earthquake location and phase identification, *Geophys. J. Int.*, *105*(2), 429–465, doi:10.1111/j.1365-246X.1991.tb06724.x.

Kiser, E., and M. Ishii (2011), The 2010 M_w 8.8 Chile earthquake: Triggering on multiple segments and frequency-dependent rupture behavior, *Geophys. Res. Lett.*, *38*(7), L07301, doi:10.1029/2011GL047140.

Kiser, E., and M. Ishii (2012), Combining seismic arrays to image the high-frequency characteristics of large earthquakes, *Geophys. J. Int.*, *188*(3), 1117–1128, doi:10.1111/j.1365-246X.2011.05299.x.

Koper, K. D., A. H. T. Lay, C. Ammon, and H. Kanamori (2011), Frequency-dependent rupture process of the 2011 M_w 9.0 Tohoku earthquake: Comparison of short-period P wave backprojection images and broadband seismic rupture models, *Earth, Planets, Space*, *63*(7), 599–602, doi:10.5047/eps.2011.05.026.

Koper, K. D., A. R. Hutko, T. Lay, and O. Sufri (2012), Imaging short-period seismic radiation from the 27 February 2010 Chile (M_w 8.8) earthquake by back-projection of P, PP, and PKIKP waves, *J. Geophys. Res.*, *117*(B2), B02308, doi:10.1029/2011JB008576.

Lay, T., L. Astiz, H. Kanamori, and D. H. Christensen (1989), Temporal variation of large intraplate earthquakes in coupled subduction zones, *Phys. Earth Planet. Inter.*, *54*(3–4), 258–312, doi:10.1016/0031-9201(89)90247-1.

Lay, T., H. Kanamori, C. J. Ammon, A. R. Hutko, K. Furlong, and L. Rivera (2009), The 2006–2007 Kuril Islands great earthquake sequence, *J. Geophys. Res.*, *114*(B11), B11308, doi:10.1029/2008JB006280.

Lay, T., C. J. Ammon, H. Kanamori, L. Rivera, K. D. Koper, and A. R. Hutko (2010), The 2009 Samoa-Tonga great earthquake triggered doublet, *Nature*, *466*(7309), 964–968.

Lay, T., H. Kanamori, C. J. Ammon, K. D. Koper, A. R. Hutko, L. Ye, H. Yue, and T. M. Rushing (2012), Depth-varying rupture properties of subduction zone megathrust faults, *J. Geophys. Res.*, *117*(B4), B04311, doi:10.1029/2011JB009133.

Li, X., G. Shao, and C. Ji (2009), Rupture process of M_w 8.1 Samoa earthquake constrained by joint inverting teleseismic body, surface waves and local strong motion, *EOS Trans. AGU*, *90*(53), U21D-03.

Maeda, T., K. Obara, T. Furumura, and T. Saito (2011), Interference of long-period seismic wavefield observed by the dense Hi-net array in Japan, *J. Geophys. Res.*, *116*(B10), B10303, doi:10.1029/2011JB008464.

Masson, D. (1991), Fault patterns at outer trench walls, *Mar. Geophys. Res.*, *13*(3), 209–225.

Masters, T., and R. Widmer (1995), Free oscillations: Frequencies and attenuations, in *Global Earth Physics: A Handbook of Physical Constants*, vol. 1, pp. 104, AGU, Washington, DC.

McFadden, P. L., B. J. Drummond, and S. Kravis (1986), The Nth-root stack: Theory, applications, and examples, *Geophysics*, *51*(10), 1879–1892, doi:10.1190/1.1442045.

Melgar, D., W. Fan, S. Riquelme, J. Geng, C. Liang, M. Fuentes, G. Vargas, R. M. Allen, P. M. Shearer, and E. J. Fielding (2016), Slip segmentation and slow rupture to the trench during the 2015, M_w8.3 Illapel, Chile earthquake, *Geophys. Res. Lett.*, *43*(3), 961–966, doi:10.1002/2015GL067369.

Meng, L., A. Inbal, and J.-P. Ampuero (2011), A window into the complexity of the dynamic rupture of the 2011 M_w 9 Tohoku-Oki earthquake, *Geophys. Res. Lett.*, *38*(7), L00G07, doi:10.1029/2011GL048118.

Meng, L., J.-P. Ampuero, Y. Luo, W. Wu, and S. Ni (2012), Mitigating artifacts in back-projection source imaging with implications for frequency-dependent properties of the Tohoku-Oki earthquake, *Earth, Planets, Space*, *64*(12), 1101–1109, doi:10.5047/eps.2012.05.010.

Meng, L., J.-P. Ampuero, and R. Bürgmann (2014), The 2013 Okhotsk deep-focus earthquake: Rupture beyond the metastable olivine wedge and thermally controlled rise time near the edge of a slab, *Geophys. Res. Lett.*, *41*(11), 3779–3785, doi:10.1002/2014GL059968.

Millen, D. W., and M. W. Hamburger (1998), Seismological evidence for tearing of the pacific plate at the northern termination of the Tonga subduction zone, *Geology*, *26*(7), 659–662, doi:10.1130/0091-7613(1998)026<0659:SEFTOT>2.3.CO;2.

Nealy, J. L., and G. P. Hayes (2015), Double point source W-phase inversion: Real-time implementation and automated model selection, *Phys. Earth Planet. Inter.*, *249*, 68–81, doi:10.1016/j.pepi.2015.09.005.

Obara, K., K. Kasahara, S. Hori, and Y. Okada (2005), A densely distributed high-sensitivity seismograph network in Japan: Hi-net by National Research Institute for Earth Science and Disaster Prevention, *Rev. Sci. Instrum.*, *76*(2), 021301, doi:10.1063/1.1854197.

Okada, Y., K. Kasahara, S. Hori, K. Obara, S. Sekiguchi, H. Fujiwara, and A. Yamamoto (2004), Recent progress of seismic observation networks in Japan: Hi-net, F-net, K-net and KIK-net, *Earth, Planets, Space*, *56*(8), 012039, doi:10.1186/BF03353076.

Okuwaki, R., Y. Yagi, and S. Hirano (2014), Relationship between high-frequency radiation and asperity ruptures, revealed by hybrid back-projection with a non-planar fault model, *Sci. Rep.*, *4*, 7120, doi:10.1038/srep07120.

Ranero, C. R., A. Villaseñor, J. Phipps Morgan, and W. Weinrebe (2005), Relationship between bend-faulting at trenches and intermediate-depth seismicity, *Geochem. Geophys. Geosyst.*, *6*(12), Q12002, doi:10.1029/2005GC000997.

Rost, S., and C. Thomas (2002), Array seismology: Methods and applications, *Rev. Geophys.*, *40*(3), 1008, doi:10.1029/2000RG000100.

Sandwell, D. T., R. D. Müller, W. H. F. Smith, E. Garcia, and R. Francis (2014), New global marine gravity model from Cryosat-2 and Jason-1 reveals buried tectonic structure, *Science*, *346*(6205), 65–67, doi:10.1126/science.1258213.

Satriano, C., E. Kiraly, P. Bernard, and J.-P. Vilotte (2012), The 2012 M_w 8.6 Sumatra earthquake: Evidence of westward sequential seismic ruptures associated to the reactivation of a N-S ocean fabric, *Geophys. Res. Lett.*, *39*(15), L15302, doi:10.1029/2012GL052387.

Tsai, V. C., M. Nettles, G. Ekström, and A. M. Dziewoński (2005), Multiple CMT source analysis of the 2004 Sumatra earthquake, *Geophys. Res. Lett.*, *32*(17), L17304, doi:10.1029/2005GL023813.

Walker, K. T., and P. M. Shearer (2009), Illuminating the near-sonic rupture velocities of the intracontinental Kokoxili M_w 7.8 and Denali fault M_w 7.9 strike-slip earthquakes with global P wave back projection imaging, *J. Geophys. Res.*, *114*(B2), B02304, doi:10.1029/2008JB005738.

Walker, K. T., M. Ishii, and P. M. Shearer (2005), Rupture details of the 28 March 2005 Sumatra M_w 8.6 earthquake imaged with teleseismic P waves, *Geophys. Res. Lett.*, *32*(24), L24303, doi:10.1029/2005GL024395.

Wang, D., and J. Mori (2011a), Rupture process of the 2011 off the pacific coast of Tohoku earthquake (M_w 9.0) as imaged with back-projection of teleseismic P-waves, *Earth, Planets and Space*, *63*(7), 603–607, doi:10.5047/eps.2011.05.029.

Wang, D., and J. Mori (2011b), Frequency-dependent energy radiation and fault coupling for the 2010 M_w8.8 Maule, Chile, and 2011 M_w9.0 Tohoku, Japan, earthquakes, *Geophys. Res. Lett.*, *38*(22), L22308, doi:10.1029/2011GL049652.

Wang, D., J. Mori, and T. Uchide (2012), Supershear rupture on multiple faults for the M_w 8.6 Off Northern Sumatra, Indonesia earthquake of April 11, 2012, *Geophys. Res. Lett.*, *39*(21), L21307, doi:10.1029/2012GL053622.

Wessel, P., and W. H. Smith (1991), Free software helps map and display data, *Eos Trans. AGU*, *72*(441), 445–446.

Wessel, P., W. H. F. Smith, R. Scharroo, J. Luis, and F. Wobbe (2013), Generic Mapping Tools: Improved version released, *Eos Trans. AGU*, *94*(45), 409–410, doi:10.1002/2013EO450001.

Wilson, J. T. (1965), A new class of faults and their bearing on continental drift, *Nature*, *207*(4995), 343–347.

Xu, Y., K. D. Koper, O. Sufri, L. Zhu, and A. R. Hutko (2009), Rupture imaging of the M_w 7.9 12 May 2008 Wenchuan earthquake from back projection of teleseismic P waves, *Geochem. Geophys. Geosyst.*, *10*(4), Q04006, doi:10.1029/2008GC002335.

Yagi, Y., A. Nakao, and A. Kasahara (2012), Smooth and rapid slip near the Japan trench during the 2011 Tohoku-Oki earthquake revealed by a hybrid back-projection method, *Earth Planet. Sci. Lett.*, *355–356*, 94–101, doi:10.1016/j.epsl.2012.08.018.

Yao, H., P. Gerstoft, P. M. Shearer, and C. Mecklenbräuker (2011), Compressive sensing of the Tohoku-Oki M_w 9.0 earthquake: Frequency-dependent rupture modes, *Geophys. Res. Lett.*, *38*(20), L20310, doi:10.1029/2011GL049223.

Yao, H., P. M. Shearer, and P. Gerstoft (2013), Compressive sensing of frequency-dependent seismic radiation from subduction zone megathrust ruptures, *Proc. Natl. Acad. Sci. U.S.A.*, *110*(12), 4512–4517, doi:10.1073/pnas.1212790110.

Yin, J., and H. Yao (2016), Rupture and frequency-dependent seismic radiation of the 2012 M_w 8.6 Sumatra strike-slip earthquake, *Geophys. J. Int.*, *205*(3), 1682–1693, doi:10.1093/gji/ggw105.

Zhou, H., Y. Wei, and V. V. Titov (2012), Dispersive modeling of the 2009 Samoa tsunami, *Geophys. Res. Lett.*, *39*(16), L16603, doi:10.1029/2012GL053068.